JGR Space Physics

RESEARCH ARTICLE
10.1029/2020JA028073

Substorm Current Wedge: Energy Conversion and Current Diversion

J. Birn[1], J. E. Borovsky[1], M. Hesse[2], and L. Kepko[3]

[1]Space Science Institute, Boulder, CO, USA, [2]Department of Physics and Technology, University of Bergen, Bergen, Norway, [3]NASA/Goddard Space Flight Center, Greenbelt, MD, USA

Key Points:
- Current diversion and generator regions of the substorm current wedge are not necessarily collocated
- Diversion to Regions 1 and 2 type currents happens inside the current wedge and equatorward of the field-aligned currents
- Azimuthally converging flows contribute to the buildup of Region 1 and Region 0 type field-aligned currents at higher latitudes

Correspondence to:
J. Birn,
jbirn@spacescience.org

Citation:
Birn, J., Borovsky, J. E., Hesse, M., & Kepko, L. (2020). Substorm current wedge: Energy conversion and current diversion. *Journal of Geophysical Research: Space Physics*, *125*, e2020JA028073. https://doi.org/10.1029/2020JA028073

Received 2 APR 2020
Accepted 30 JUN 2020
Accepted article online 16 JUL 2020

Abstract Using a magnetohydrodynamic simulation of magnetotail reconnection, flow bursts, and dipolarization, we further investigate the current diversion and energy flow and conversion associated with the substorm current wedge (SCW) or smaller-scale wedgelets. Current diversion into both Region 1 (R1) and Region 2 (R2) sense systems is found to happen inside (that is, closer to the center of the flow burst) and equatorward of the R1 and R2 type field-aligned currents. In contrast to earlier investigations the current diversion takes place in dipolarized fields extending all the way toward the equatorial plane. An additional FAC system with the signature of Region 0 (R0) (same sense as R2) is found at higher latitudes in taillike fields. The diversion into this system takes place in layers equatorward of the R0 currents but outside the equatorial plane. Whereas the diversion into R1 and R2 systems is pressure gradient dominated, the diversion into the R0 system is inertia dominated and may persist only during flow burst activity. While azimuthally diverging flows near the dipole contribute to the buildup of R1 and R2 systems, converging flows at larger distance contribute to the buildup of R0 and R1 systems. In contrast to the current diversion regions inside the current wedge, generator regions are found on the outside of the wedge, similar to earlier results. Within the tail domain covered, these regions are overpowered by load regions, such that additional generator regions must be expected closer to Earth, not covered by the present simulation.

1. Introduction

One of the most intriguing problems in magnetospheric physics is the question how magnetotail dynamics and characteristic features drive auroral phenomena. This is largely an unsolved problem. Yet, one of the best understood relationships is that between flow bursts in the magnetotail and auroral streamers. It has been realized that the connection is carried by outward field-aligned current (FAC) created at the westward edge of an earthward flow channel in the tail (e.g., Forsyth et al., 2008; Henderson et al., 1998; Lyons et al., 1999; Nakamura, Baumjohann, Brittnacher et al., 2001; Nakamura, Baumjohann, Schödel et al., 2001; V. A. Sergeev et al., 1999; V. Sergeev et al., 2004). This current is part of a system that, albeit on a smaller scale, resembles that of the substorm current wedge (SCW) (McPherron et al., 1973). Its major component consists of a diversion of cross-tail current into FAC, earthward on the dawnside and tailward on the duskside, associated with a collapse and dipolarization of magnetic field in a some tail section in between, combined with an ionospheric closure through the westward auroral electrojet. The FACs associated with this simple current loop have the characteristics of those denoted as "Region 1" (R1) (Iijima & Potemra, 1976).

The likely mechanism for the buildup of this current system is the vorticity or flow shear on the outside of a flow burst. This relationship has been supported by many magnetohydrodynamic (MHD) simulations (e.g., Birn & Hesse, 1991; Birn et al., 2011; Merkin et al., 2019; Scholer & Otto, 1991; Wiltberger et al., 2015) and observations (e.g., Forsyth et al., 2008; Keiling et al., 2009; Liu et al., 2013). The basic mechanism is illustrated in Figure 1, modified from Figure 19 of Birn et al. (2004) and Figure 3.7a of Amm et al. (2002). A flow burst from the tail is stopped closer to Earth and diverted azimuthally. The shear or vorticity on the outside causes a twisting of magnetic flux tubes, which increases as long as the ionosphere does not, or not fully, respond to the driving vortical flow. This twist and the associated currents might persist even when the flow subsides, depending on the ionospheric dissipation.

The simple, cylindrically symmetric, cartoon in Figure 1b would suggest that the regions of current diversion (from perpendicular to field-aligned or vice versa) and generator regions, where $\mathbf{E}\cdot\mathbf{j} < 0$, are closely related. It

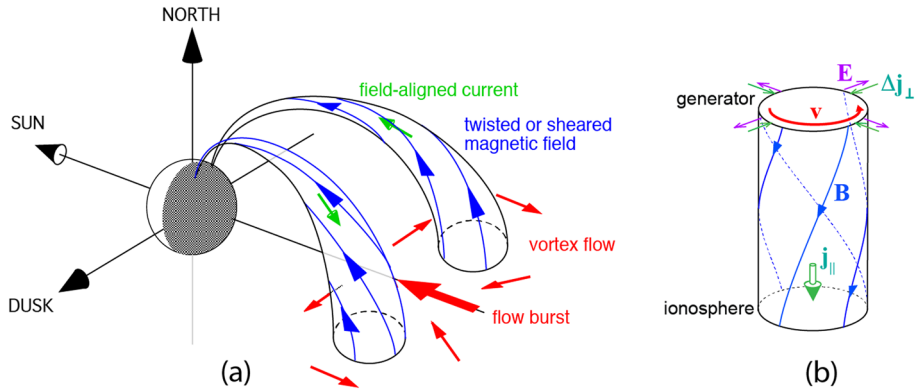

Figure 1. Field-aligned current generation by vortical plasma flow: (a) magnetic flux tubes in the Northern Hemisphere, after Figure 1 of Birn and Hesse (2013); (b) simple cartoon representing the twist on the dawnside, similar to Figure 3.7a of Amm et al. (2002).

is the purpose of this paper to investigate details of the current diversion and their relation to generator or dynamo regions in the magnetotail on the basis of an MHD simulation of magnetotail reconnection, associated with flow bursts and dipolarization (Birn et al., 2011). This simulation has been used previously to study properties of the SCW (Birn & Hesse, 2013, 2014b). We should note here that this simulation, and in particular the first flow burst, may also be applicable to a smaller-scale flow channel, which may be part of, or independent of, substorm activity. We should further note that this driving mechanism could, on even smaller scales, also be applicable to electron flows as drivers of auroral arcs

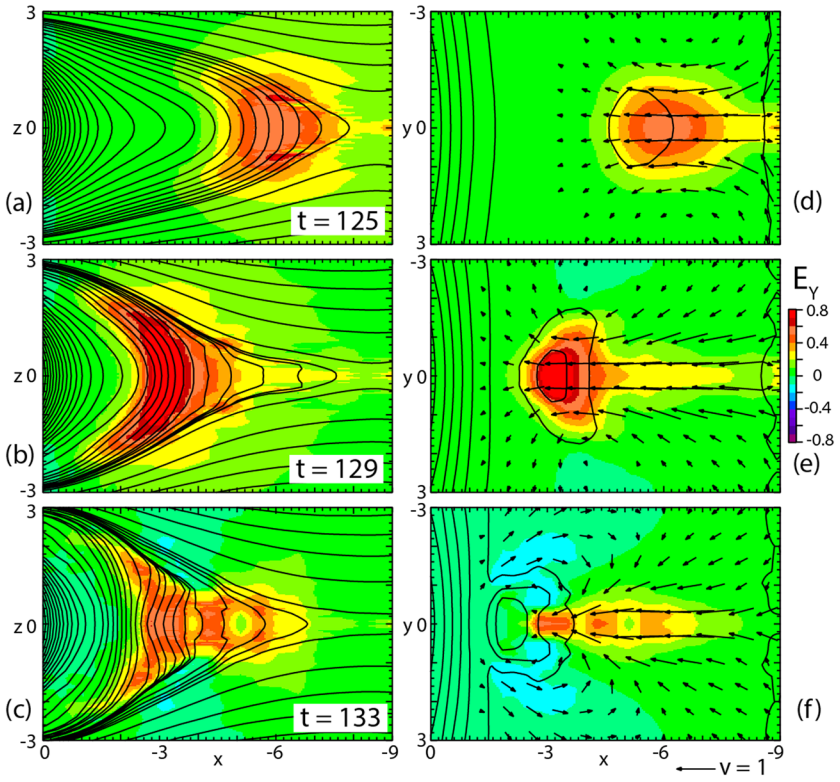

Figure 2. Evolution of the cross-tail electric field E_y (color): (a–c) in the x,z plane together with magnetic flux contours, and (d–f) in the x,y plane together with contours of constant B_z (solid black lines), shown in increments of 0.5 (10 nT) from $B_z = 0$ on the right. Black arrows are velocity vectors with the unit vector (1,000 km/s) shown at the bottom right.

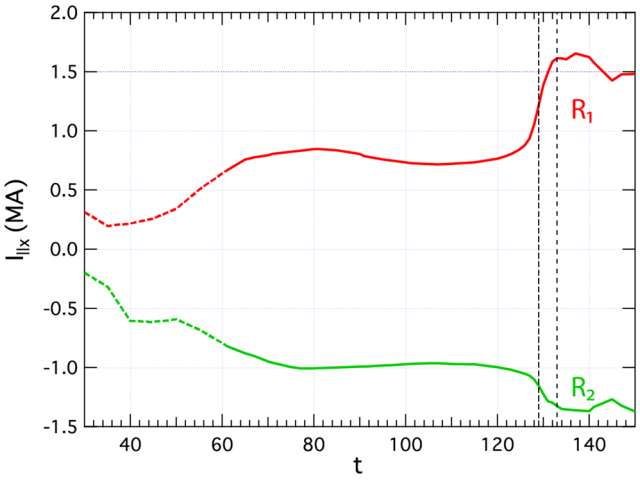

Figure 3. Evolution of the total current of Region 1 (positive, red curve) and Region 2 signature (negative, green curve), integrated for $y<0, z>0$ within the close field line region; modified after Figure 2 of Birn and Hesse (2014b). The dashed vertical lines indicate times for which energy flow and conversion ($t=129$) and current diversion ($t=133$) are investigated.

(e.g., Amm et al., 2002; Borovsky et al., 2020). In the following section we will briefly describe properties of the MHD simulation. Section 3 is devoted to details of energy flow and conversion, while section 4 addresses details of the spatial properties of the current diversion from perpendicular to field aligned. This is followed by discussion (section 5) and summary (section 6).

2. MHD Simulation

Major properties of the MHD simulation are described by Birn et al. (2011) and Birn and Hesse (2013) but will be partially repeated here, for the readers' convenience. The simulation is based on dimensionless quantities with suitable units given by

$$L_n = 10,000\ \text{km} \approx 1.5R_E, \quad B_n = 20\ \text{nT}, \quad v_n = 1,000\ \text{km/s} \qquad (1)$$

This leads to derived units $t_n = L_n/v_n = 10\,\text{s}$, $p_n = B_n^2/\mu_0 = 0.32$ nP, $j_n = B_n/(\mu_0 L_n) = 1.6\ \text{nA/m}^2$, and $I_n = B_n L_n/\mu_0 = 0.16$ MA. The simulation box spans the region $0 > x > -60$, $|y|<40$, $|z|<10$ (corresponding to $-7.5R_E > x_{GSM} > -97.5R_E$, $|z_{GSM}|<15R_E$, $|y_{GSM}|<60R_E$). The initial state consisted of a tail field (Birn, 1987) with a superposed three-dimensional dipole with a center located at $x=+5$ outside the simulation box. The configuration includes a small net cross-tail field component of a few percent of the lobe field, which breaks mirror symmetry but satisfies rotational symmetry for 180° rotation around the x axis.

The evolution consists of a relaxation phase ($0<t<30$, corresponding to 300 s), during which the system relaxed into full equilibrium (Hesse & Birn, 1993), followed by a driven phase ($30<t<61$), during which an external inflow of magnetic flux was applied to the top and bottom boundaries. This leads to current intensification and the formation of a thin embedded current sheet in the near tail. At $t=61$ the driving was stopped and finite resistivity was imposed, concentrated in the region of enhanced current density, leading to the onset of reconnection and the formation of a neutral line ($B_z=0$ at $z=0$) at $t\approx 90$.

Rapid reconnection, driving a fast flow burst, starts at $t\approx 125$. The evolution of this flow burst is illustrated in Figure 2, showing in color the associated cross-tail electric field E_y. Figures 2a–2c show E_y in the x,z plane together with magnetic flux contours, while Figures 2d–2f show E_y in the x,y plane together with velocity vectors and contours of constant B_z; the contour on the right is the $B_z=0$ line. The flow reaches a peak at $t\approx 129$ and is slowed down considerably at $t=133$, while being diverted azimuthally and even tailward. The indented field lines shown in Figure 2c indicate that this is related to a reversal of the cross-tail current, causing a repulsive tailward $\mathbf{j}\times\mathbf{B}$ force.

The shear associated with this flow burst causes a buildup of FAC as illustrated in Figure 1. Figure 3 shows the evolution of the total FACs of R1 and, oppositely directed Region 2 (R2) sense, evaluated at the inner boundary $x=0$ for $y<0, z>0$. These currents show a significant rise after the onset of the fast flow and a saturation when the flow is stopped and even reversed.

The two dashed lines indicate times for which we investigate the energy flow and conversion and the current diversion in more detail; they correspond to the two bottom panels in Figure 2. We note that our limited tail simulation does not include the possibility of ionospheric dissipation and a potential balance with a tail generator. Therefore, for the energy transport and conversion (discussed in section 3), and, particularly for the identification of potential generator or dynamo regions, we choose a time ($t=129$) at which the buildup of the current systems is the strongest. For the current diversion (section 4) we choose the time $t=133$, when the FACs have saturated.

3. Energy Flow and Conversion

Figure 4 provides an overview of the major energy flow and conversion, showing the color-coded energy conversion term $\mathbf{E}\cdot\mathbf{j}$, (a) as function of x and z, integrated over $|y|<1$, and (b) as function of x and y, integrated

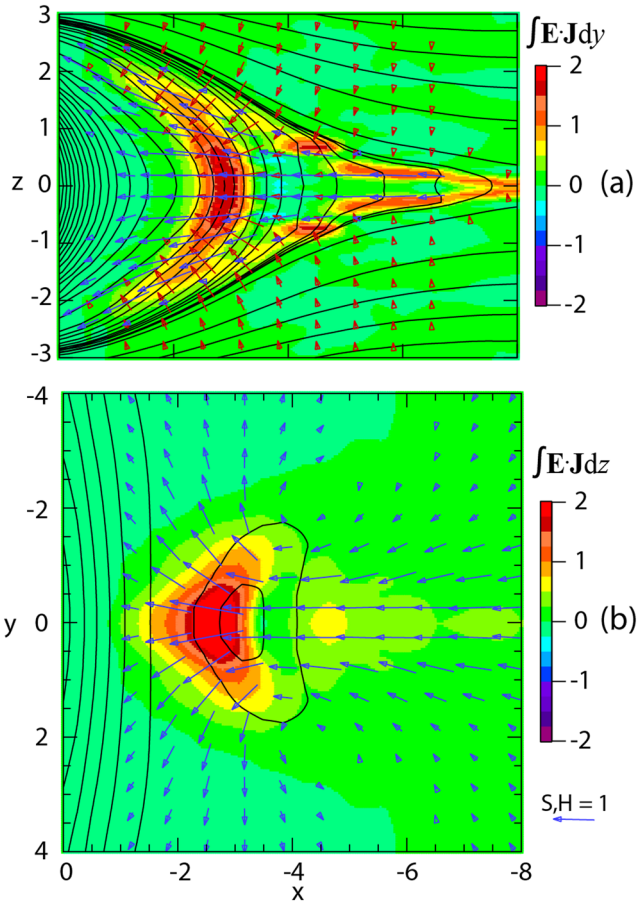

Figure 4. Color-coded energy conversion term $\mathbf{E}\cdot\mathbf{j}$ at $t = 129$, shown (a) as a function of x and z, integrated over $|y| < 1$, and (b) as a function of x and y, integrated over $|z| < 3$. Red arrows in Panel (a) indicate Poynting vectors, and blue arrows in Panels (a) and (b) show enthalpy flux vectors; the unit vector, equivalent to $1.3 \times 10^{10} J/R_E^2/s$, which is the same for both, is indicated at the bottom right. Only vectors with a minimum magnitude of 0.05 are shown. Black contours in Panel (b) are contours of constant B_z, shown at intervals of 0.5 (10 nT) above 0.

over $|z| < 3$, together with Poynting vectors $\mathbf{S}$ (red arrows) and enthalpy flux vectors $\mathbf{H}$ (blue arrows) defined by

$$\mathbf{S} = \mathbf{E} \times \mathbf{B} \qquad \mathbf{H} = \frac{5}{2} p\mathbf{v} \tag{2}$$

assuming a polytropic index $\gamma = 5/3$ (using standard notations). We note that the enthalpy flux vectors show the direction of the total flow, while the Ponting vectors show the flow direction perpendicular to the magnetic field, which, however, in the lobe regions is close to the actual flow direction.

As demonstrated already in Birn and Hesse (2005), energy is released from the lobes into Poynting flux and enters the inner tail over a wide region earthward of the x line, which is located near $x = -8.5$. The Poynting flux is converted predominantly into enthalpy flux at slow shock like current layers. This is associated with $\nabla\cdot\mathbf{S} < 0$ and $\nabla\cdot\mathbf{H} > 0$ (not shown here). It is documented also in particle-in-cell simulations with small or no guide field (e.g., Birn & Hesse, 2010, 2014a). A similar conversion layer appears to be associated with the dipolarization front (DF) just earthward of the region of enhanced B_z. However, its character is quite different. Whereas the slow shocks are quasi-stationary, associated with a flow across, the DF does not not exhibit cross flow; it merely separates two distinctly different regions and $\mathbf{E}\cdot\mathbf{j} > 0$ results from the fact that large magnetic field (high Poynting flux) is transported earthward into a fixed box and low field transported out, while the opposite is true for the enthalpy flux. Figure 4b indicates that closer to Earth enthalpy flux (and plasma flow) is diverted azimuthally and even tailward.

Figure 5 provides an overview of the energy flow and conversion in a cross section at $x = -2$. Panel (a) shows the enthalpy flux component H_x, Panel (b) the Poynting flux S_x, and Panel (c) the conversion term $\mathbf{E}\cdot\mathbf{j}$, together with Poynting vectors (black arrows). Note that the color scale in Panel (c) is chosen to emphasize the generator regions $\mathbf{E}\cdot\mathbf{j} < 0$; the maximum positive values at the center are larger by a factor of about 4. The vector at the bottom right of Figure 5c shows the unit Poynting flux, corresponding to $1.3 \times 10^{10} J/R_E^2/s$. Figures 5d–5h show quantities only for the generator region in the quadrant $y < 0, z > 0$.

The energy flux vectors in Figures 4b and 5a–5c demonstrate that the energy that is fed into a flow burst and DF stems from a much wider region in y than the actual front or burst. Figure 5 also demonstrates that the vortical flow that causes the buildup of the current wedge persists closer to Earth. As discussed by Birn and Hesse (2005), the generator regions are associated with an outward flow component toward larger $|z|$, consistent with the cartoon in Figure 1b. This is associated with $\nabla\cdot\mathbf{S} > 0$ (Figure 5d) and $\nabla\cdot\mathbf{H} < 0$ (not shown), representing the conversion of thermal energy to magnetic energy flux. However, inspection of the contributions to $\nabla\cdot\mathbf{S}$ in Figures 5d–5g shows that the dominant term stems from $\partial S_z/\partial z$. That means that there is only a small conversion to earthward Poynting flux (Figure 5h). It is smaller than the Poynting flux near midnight (Figure 5b) by a factor of about 5, which again is smaller than the enthalpy flux (Figure 5a) by a factor of about 4.

Figure 6 is an attempt to put the driving of the FACs and the generator regions at $t = 129$ into a three-dimensional view. The inner plane $x = 0$ shows the color-coded values of $j_{||}$, indicating both R1 (red and yellow) and R2 (blue) type currents. A contour of constant $j_{||}$ (black contour) is mapped into the equatorial plane $z = 0$; five field lines of this mapping are indicated as red lines. The color in the equatorial plane $z = 0$ indicates the magnitude of the vorticity, $\boldsymbol{\Omega} = \nabla \times \mathbf{v}$, multiplied with the magnitude of B_z, and black arrows show the flux transport vectors $B_z\mathbf{v}$. This shows that the central region of fast flow and strong vorticity is

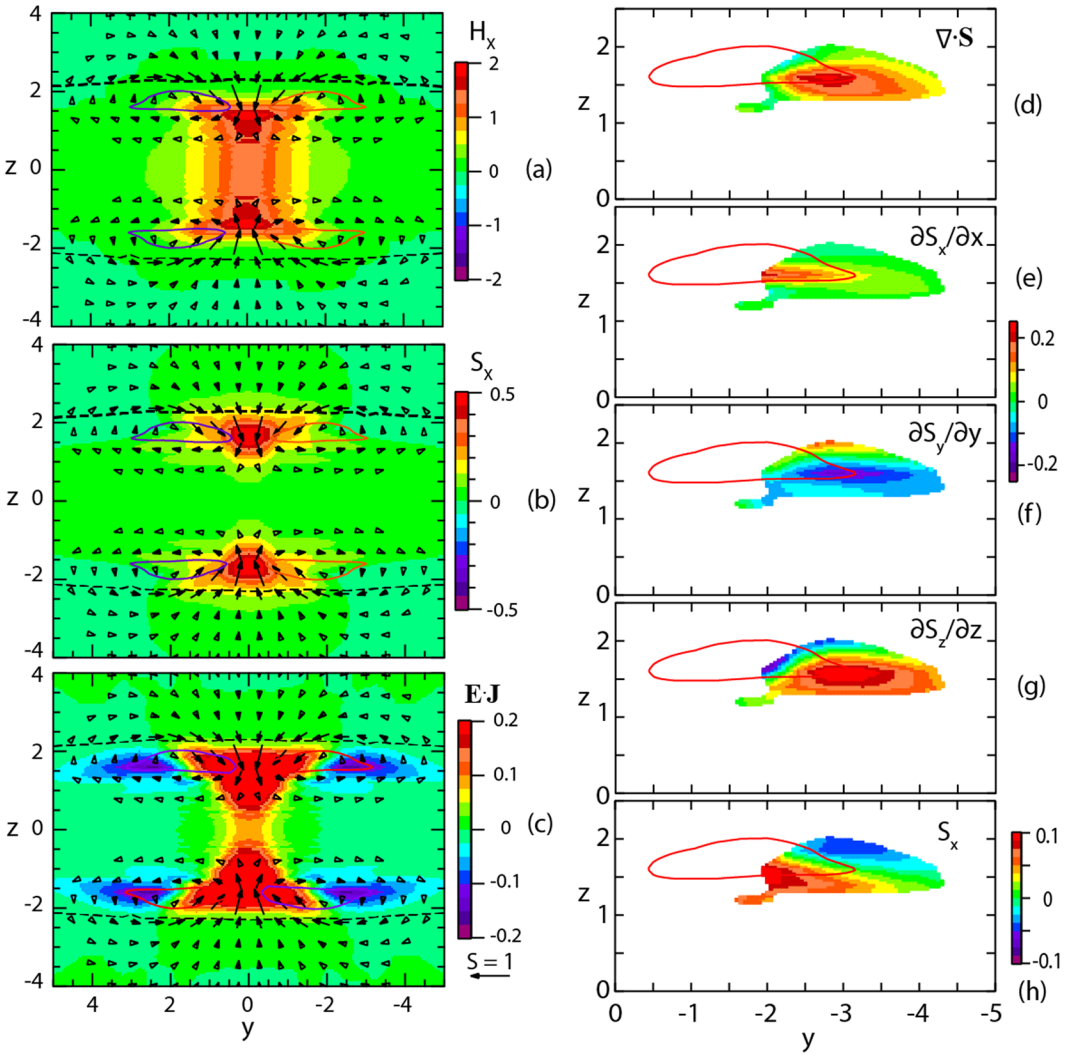

Figure 5. Energy fluxes and conversion at $x = -2$ for $t = 129$: (a) color-coded enthalpy flux H_x, (b) Poynting flux S_x, and (c) energy conversion term $\mathbf{E}\cdot\mathbf{j}$. Note that the color scale in Panel (c) is chosen to emphasize the generator regions $\mathbf{E}\cdot\mathbf{j} < 0$. Black arrows show Poynting vectors; the unit vector is indicated at the bottom right. Colored contours indicate R1 sense field-aligned currents, and the dashed black lines represent the open-closed boundary (separatrix). Panels (d–h) show quantities in the generator region, selected for $\mathbf{E}\cdot\mathbf{j} < -0.05$ in the quadrant $y < 0, z > 0$: (d) the divergence of the Poynting vector, $\nabla\cdot\mathbf{S}$, (e–g) the individual contributions to $\nabla\cdot\mathbf{S}$, and (h) again the Poynting vector component S_x but on a different color scale.

predominantly responsible for the distortion of the magnetic field; it is consistent with the location of the main current diversion, to be discussed in section 4.

In addition, Figure 6 shows the generator regions $\mathbf{E}\cdot\mathbf{j} < 0$ in planes $x = -1, -2, -3$ (located on the outside of the R1 current region), and $x = -4$ (located near midnight). The region at $x = -2$ corresponds to that shown in Figure 5c and selected for Figures 5d–5h. The midnight region of negative $\mathbf{E}\cdot\mathbf{j}$ at $x = -4$ results from flow braking, causing a reversal of current as indicated in Figure 2c. This effect becomes stronger at later times when, however, the FACs are already saturated.

4. Current Diversion

Next, we provide an overview of the spatial distribution of FACs at the chosen time of saturation, $t = 133$. As indicated by Figure 2, at this time the flow burst has slowed down considerably and become strongly diverted. It stops near midnight at $x \approx -3$, and earthward flow is confined to approximately $|y| < 1$.

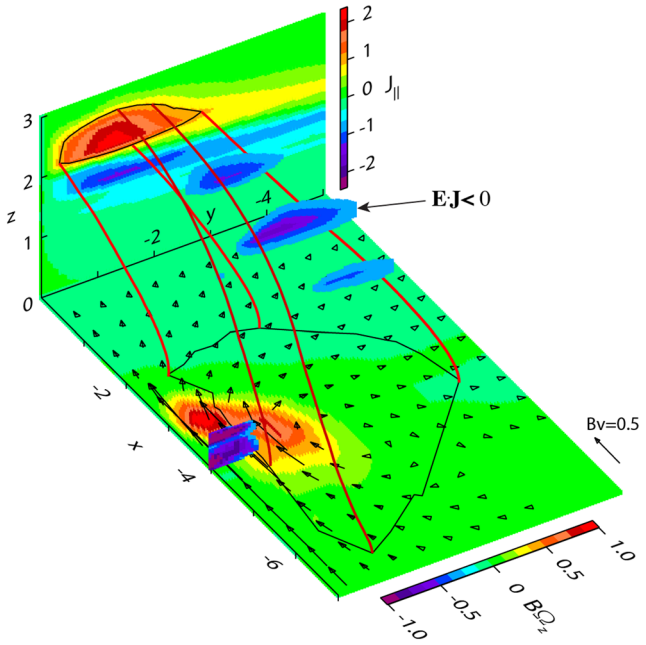

Figure 6. Perspective view of the driving and generator mechanisms of the current wedge at $t = 129$. The plane at $x = 0$ shows the color-coded field-aligned current; red lines represent field lines mapped from from an outer contour (black) into the equatorial plane. The color in the equatorial plane $z = 0$ indicates the magnitude of the vorticity, multiplied with the magnitude of B_z, and black arrows show the flux transport vectors $B_z\mathbf{v}$; the arrow at the bottom right shows a magnitude of 0.5, corresponding to 10^4 nT km/s. Generator regions $\mathbf{E}\cdot\mathbf{j} < 0$ are shown in planes $x = -1,-2,-3$ (outer regions), and $x = -4$ (near midnight).

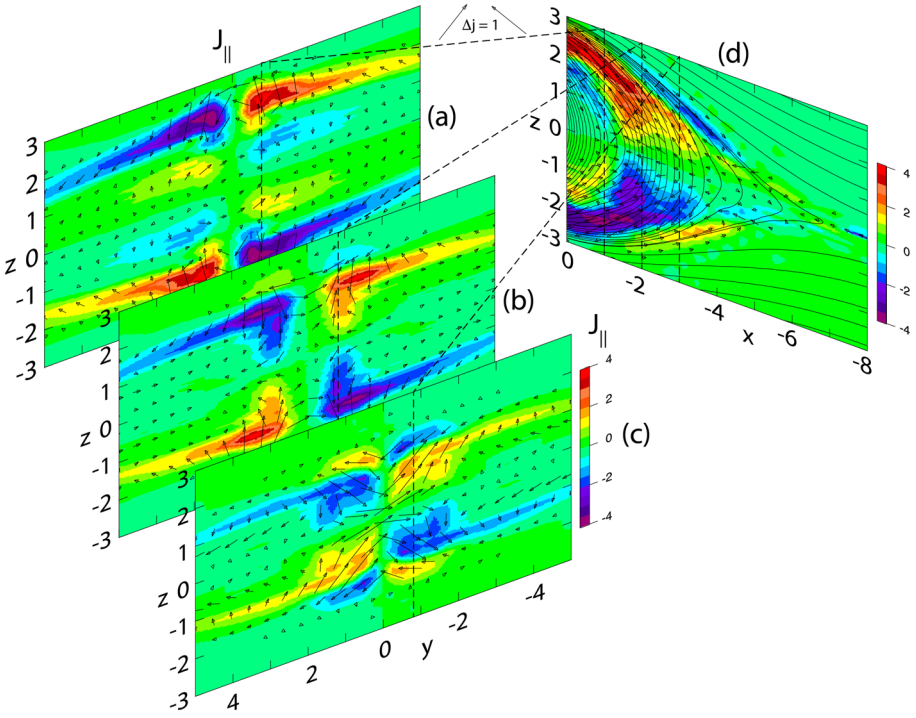

Figure 7. Color-coded field-aligned current density $j_{||}$ at three locations in x (Panels a–c) and at $y = -0.8$ (Panel d) as indicated. The arrows show perturbed current density vectors. The two arrows at the top show unit vectors, corresponding to 1.6 nT/m^2, for the left and right panels, respectively; they are not quite identical in length due to the different distortions of the projections. Black lines in Panel (d) are magnetic flux contours.

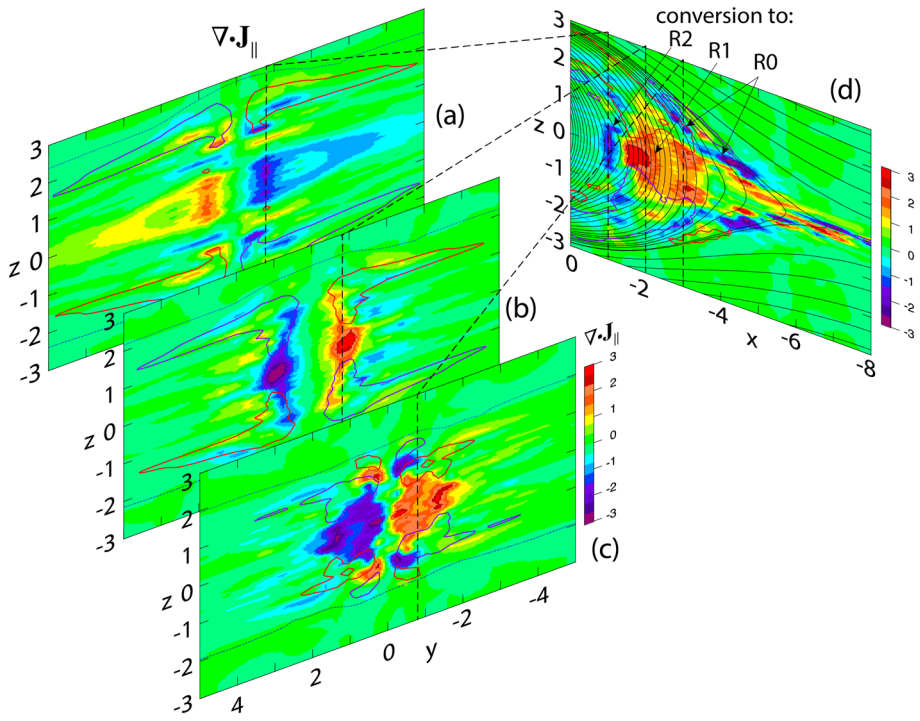

Figure 8. Color-coded divergence of field-aligned currents $\nabla\cdot\mathbf{j}_{||}$, with contours outlining the field-aligned currents shown in Figure 7 (colored lines). Black arrows in Panel (d) point to regions of conversion to R2, R1, and R0 type currents, respectively.

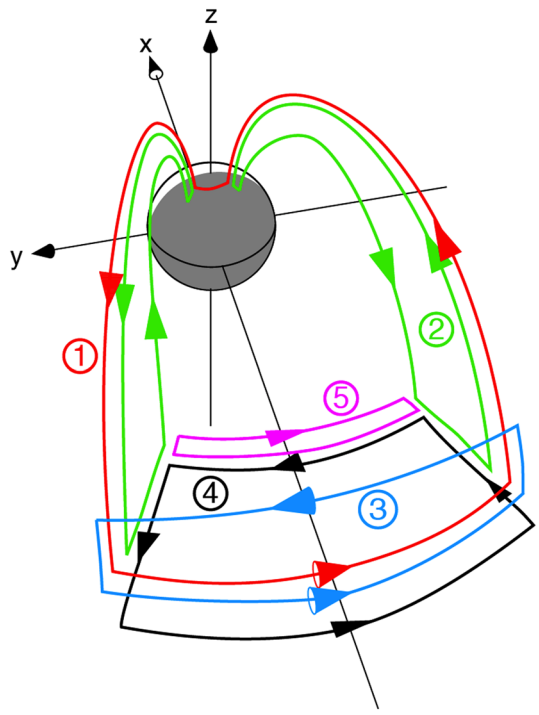

Figure 9. Schematic of major current systems contributing to the SCW, after Birn and Hesse (2014b).

Figure 7 shows the color-coded current density, $j_{||} = \mathbf{j}\cdot\mathbf{B}/|\mathbf{B}|$, in planes $x = -1,-2,-3$ (Panels a–c) and $y = -0.8$ (Panel d). The arrows in each of the planes show perturbed current density vectors $\Delta\mathbf{j}$, defined by subtracting the current density vectors at the initial time $t = 61$, $\Delta\mathbf{j} = \mathbf{j}(133)-\mathbf{j}(61)$.

Figure 7 shows the dominant R1 type currents, flowing toward the Earth on the dawn side (red for $z > 0$ and blue for $z < 0$) and away on the dusk side, and at lower latitude the oppositely directed weaker R2 type currents. Figures 7c and 7d also show, at higher latitude, FACs with the same direction as R2, already indicated in Figure 8 of Birn and Hesse (2014b). This system, which may be identified as Region 0 (R0), does not extend to the inner boundary. Local signatures of such a system, however, have been reported by Nakamura et al. (2017, 2018).

Figure 8 shows the corresponding divergence of FACs, defined by $\nabla\cdot\mathbf{j}_{||} = \mathbf{B}\cdot\nabla(j_{||}/|B|)$, with $\mathbf{j}_{||} = j_{||}\,\mathbf{B}/B$. The red areas in Figures 8b and 8c (for $y < 0$) and Figure 8d demonstrate that the conversion to R1 type FACs happens on the inside (that is, for smaller $|y|$ and underneath (that is, for smaller $|z|$) the R1 currents. This is also confirmed by the perturbed current vectors in Figures 7b and 7c, which point dawnward across midnight and toward larger $|z|$ in Figure 7d into the regions of R1 currents. These current density vectors indicate Current Loops 1 and 3 in Figure 5 of Birn and Hesse (2014b), which is reproduced in Figure 9. Both the perturbed current density vectors and the divergence of FACs, given by $\nabla\cdot\mathbf{j}_{||}$, shown in Figure 8, demonstrate that the current deflection to parallel current happens inside the wedge, from perturbed perpendicular currents that oppose the original cross-tail current, rather than on the outside as the original cartoon by McPherron et al. (1973) might suggest.

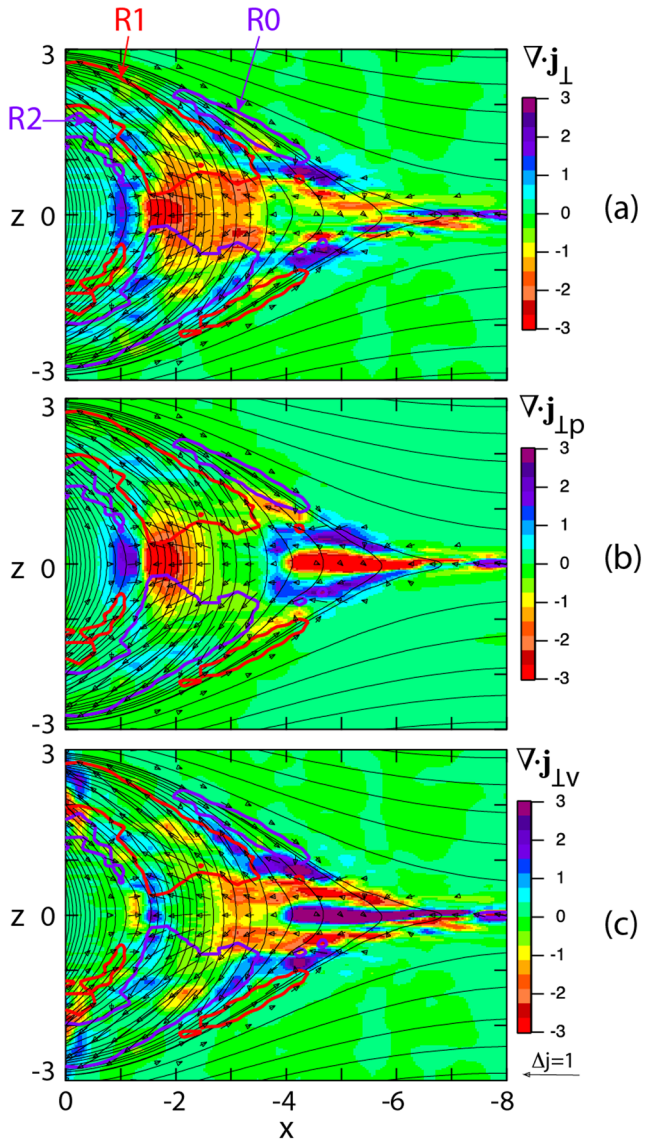

Figure 10. Divergence of perpendicular currents and perturbed current density vectors at $y = -0.8$, corresponding to the right panel in Figure 8, (a) total, (b) contribution from pressure gradients, (c) contribution from inertia. Colored contours show the regions of R2, R1, and R0 currents, respectively, as indicted in Panel (a). The arrow at the bottom right represents the unit current density vector, corresponding to 1.6 nA/m^2.

Current diversion into both R1 and R2 systems extends all the way toward the equatorial plane. This is in contrast to earlier findings (Birn & Hesse, 2005), where the diversion into R1 sense currents was found to occur in layers roughly parallel to the equatorial plane, located underneath the current layers at lower $|z|$, but away from the equatorial plane. The main reason for this difference is that the earlier simulation was based on a taillike configuration, whereas the present one also includes the transition toward a dipole field, such that current diversion into R1 and R2 systems takes place in dipolarized fields, which are predominantly northward. This conclusion is supported by the fact that, in contrast to the diversion into R1 and R2 systems, the diversion into the R0 system takes place in more taillike fields in layers underneath, at lower $|z|$, but away from the equatorial plane (Figure 8d).

To provide further insight into the current diversion, we have investigated the contributions to $\nabla\cdot\mathbf{j}_\perp\,(=-\nabla\cdot\mathbf{j}_\parallel)$ from pressure gradients and inertia, as defined by

$$\mathbf{j}_\perp = \frac{\mathbf{B}}{B^2}\times\left(\nabla p + \rho\frac{d\mathbf{v}}{dt}\right) \tag{3}$$

Figure 10 shows the total contribution to $\nabla\cdot\mathbf{j}_\perp$ and the individual contributions in the plane $y = -0.8$. For better comparison with Figure 8 we have reversed the color scale. Thus, Figure 10a is identical to Figure 8d, since $\nabla\cdot\mathbf{j}_\perp = -\nabla\cdot\mathbf{j}_\parallel$.

Obviously, R2 currents are predominantly "pressure driven" (Figure 10b). Also, the inner portion of the divergence to R1 currents is pressure gradient dominated. However, further tailward there is also a contribution from inertia, which feeds into the higher-latitude portion of the R1 current. This part, together with the diversion to R0 currents at even higher latitude, was obscured in our previous analysis (Birn & Hesse, 2014b) by the integration over z. In contrast, the diversion to R0 currents appears entirely "inertia driven." Therefore, this current might persist only as long as the flow burst activity persists in the tail. As noted before, signatures of this current have been identified by tail observations (Nakamura et al., 2017, 2018). Below, that is, equatorward of, the region of conversion to R0 currents, and tailward of $x \approx -4$ there is a region where pressure gradient and inertia associated diversion terms largely compensate. This is related to an approximate balance of pressure gradient forces and inertia and a conversion of bulk flow energy, which is significant near the x line, to enthalpy flux in the reconnection outflow toward increasing pressure.

Figure 11 provides a perspective view of the field distortion at this time, similar to Figure 6. It shows again field lines (red lines) extending from an outer contour of the R1 region at $x = 0$ into the equatorial plane $z = 0$. The color at $z = 0$, however, now indicates the magnitude of $\nabla\cdot\mathbf{J}_\parallel$, integrated over z, while black arrows show again the flux transport vectors $B_z\mathbf{v}$. In addition, the thick multicolored line represents a field line crossing the region of negative B_y and the R0 current region; the color indicates the magnitude of $J_\parallel$ along this line. It is obvious that this field line and its neighbors have become distorted by converging flow toward midnight at larger distance and subsequent earthward flow. This has caused the buildup of negative B_y. Below this region, that is, at lower z, this causes a gradient $\partial B_y/\partial z < 0$, corresponding to earthward current, while above, that is, at larger z, this causes a gradient $\partial B_y/\partial z > 0$, corresponding to tailward current. The converging flow toward midnight at the tailward side of the vortex pattern in the equatorial plane therefore contributes to both R1 and R0 current buildup. This is analogous to the diverging flow away from midnight on the earthward side of the

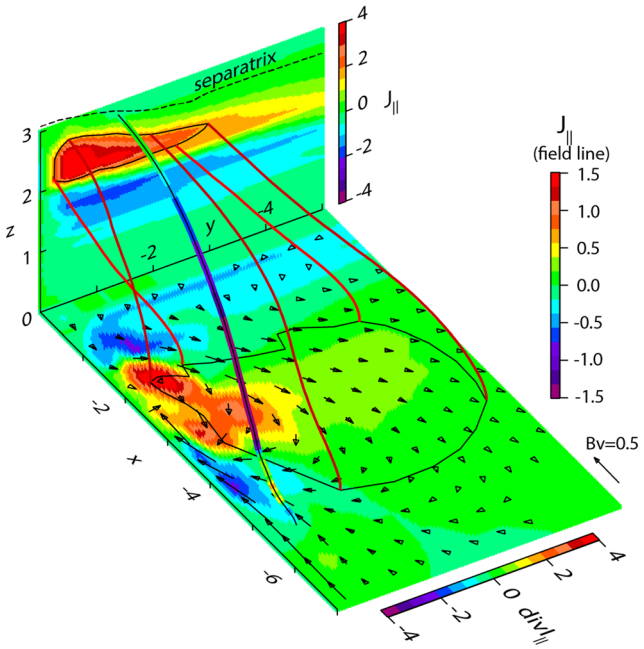

Figure 11. Perspective view of the field distortions associated with the current wedge at $t = 133$, similar to Figure 6. The plane at $x = 0$ again shows the color-coded field-aligned current; red lines represent field lines mapped from an outer contour (black) into the equatorial plane. The color in the equatorial plane $z = 0$; however, it now indicates the magnitude of $\nabla\cdot\mathbf{J}_{\|}$, integrated over z, while black arrows show again the flux transport vectors $B_z\mathbf{v}$; the arrow at the bottom right shows a magnitude of 0.5, corresponding to 10^4 nT km/s. The thick multicolored line represents a field line crossing the region of negative B_y and the R0 type current region; the color indicates the magnitude of $J_{\|}$ along this line, indicated by the color bar to the right.

vortex, which causes a buildup of R1 and R2 currents. Although the R0 type current does not extend to the boundary at this time, one might expect that the associated field perturbation travels toward Earth and might be related to observed R0 type currents as depicted in Figure 9 of Kepko et al. (2015), based on observations by Dynamics Explorer satellites and cartoons by Fujii et al. (1994) (Figure 11) and Gjerloev and Hoffman (2002). Note that Figure 9 of Kepko et al. (2015) and Figure 11 of Fujii et al. (1994) also indicate the converging plasma flows toward midnight at high latitude, although one ought to be cautious, because electric fields and currents in the ionosphere can be distorted by the anisotropic conductivity.

5. Discussion

The most puzzling aspect of the present investigation concerns the question of how the energy that is ultimately dissipated by current closure in the ionosphere is generated by dynamo action in the tail or the inner magnetosphere. A common way of investigation is the identification of regions of $\mathbf{E}\cdot\mathbf{j} < 0$ (although it should be noted that this quantity is frame dependent). The present simulation does not include the presumed ionospheric dissipation region and the possible balance between the generator in the tail and the dissipator. We therefore focused on a time of the rapid buildup of the SCW system and identified generator regions of $\mathbf{E}\cdot\mathbf{j} < 0$ at the outside (in $|y|$) of the R1 type FAC system at higher latitudes and in the center of the tail at a braking region just behind the earthward moving DF. However, the high-latitude region is weak, and it turns out that the main contribution to $\nabla\cdot\mathbf{S}$ stems from $\partial S_z/\partial z$, which means it does not significantly contribute to a conversion to earthward Poynting flux. The central region is located behind, that is, tailward of, the DF region, where $\nabla\cdot\mathbf{S} < 0$ and $\nabla\cdot\mathbf{H} > 0$ and thus also does not contribute to an increase in net earthward Poynting flux. Although this region becomes stronger at later times, when the DF is stopped, that happens when the R1 and R2 currents, set up by the first flow burst, are already saturated. Thus, none of these generator regions can realistically be considered as the dynamo that drives the R1 current of the current wedge.

Thus, although the flows and the current diversion in the present simulation are sufficient to represent the source region of the SCW, they apparently do not contain the main generator. How can we explain this contradiction? The solution lies in the fact that the SCW system, although dominant in the connection between tail and ionosphere, is only part of the total current system. If the Current Loop 1 in Figure 9 were the only one, it would be easy to identify the dynamo ($\mathbf{E}\cdot\Delta\mathbf{j} < 0$) in the central, near-equatorial portion of dusk-to-dawn current together with the earthward flow, which is associated with dawn-to-dusk electric field. However, this current is superposed on the preexisting cross-tail current (apart from other systems indicated in Figure 9), and the energy equations are nonlinear and do not permit a separation into different current circuits. It is therefore not possible to identify drivers or dynamos of subsystems by investigating $\mathbf{E}\cdot\mathbf{j} < 0$.

Nevertheless, it is useful to investigate the energy flow and conversion. There is no doubt that the ultimate source is the lobe magnetic energy (or prior to that, the solar wind energy that is temporarily stored in the tail). The initial release and conversion of this energy is relatively clear: Magnetic energy is released by Poynting flux and converted largely to enthalpy flux at slow shocks or their equivalent, characterized by $\mathbf{E}\cdot\mathbf{j} > 0$. A small amount that is converted to bulk kinetic energy flux in the vicinity of the x line is also mostly converted to enthalpy flux farther earthward when the reconnection outflow is braked by moving toward increasing pressure. A further transformation by $\mathbf{E}\cdot\mathbf{j} > 0$ takes place at DFs. However, this is essentially a frame dependent phenomenon, which, at least in the MHD limit, results from the transport of a flux bundle with enhanced magnetic field B_z (and associated enhanced electric field E_y), rather than a dissipation process

acting in frame moving with the DF. Both of these mechanisms, however, are also present in purely two-dimensional pictures and simulations (e.g., Birn & Hesse, 2014a; Liu et al., 2014; Sitnov et al., 2009) and are hence not necessarily related to the SCW and its ionospheric closure.

The generator regions of $\mathbf{E}\cdot\mathbf{j} < 0$ found in this simulation at the outside of the R1 type FAC system, consistent with observations (Hamrin et al., 2006; Marghitu et al., 2006), are a purely 3-D effect, while the braking region near midnight would also be present in 2-D. As discussed above, however, they are not sufficient to explain the ultimate conversion to earthward Poynting flux that is expected prior to entry into the ionosphere. Our estimates of the total energy transport from the tail (Birn et al., 2019) indicate that this energy would be sufficient to cover the ionospheric dissipation in a substorm. However, this estimate does not account for the energy deposited in the ring current, and only a small amount is found to be converted to Poynting flux by dynamo action in the tail region considered here. Since this energy conversion is not sufficient, we must conclude that the major conversion of enthalpy flux to Poynting flux must happen further earthward.

6. Summary and Conclusions

Using a three-dimensional MHD simulation of magnetotail reconnection and dipolarization (Birn et al., 2011), we have investigated details of energy release and conversion and current diversion associated with the SCW or a single flow burst driving a similar current system, extending further the investigations of Birn and Hesse (2013, 2014b). These currents consist of a dominant FAC system, which is earthward on the dawnward side of the flow burst and tailward on the duskward side, denoted here as R1 system, and a secondary system of opposite sense, generated closer to Earth at lower latitudes, denoted as R2 system. These notations reflect the notations as R1 and R2 of the statistical study of Iijima and Potemra (1976), consistent with the fact that the flow burst investigated in this paper is initiated near midnight. We note, however, that similar current systems may exist in relation to flow bursts that are generated off midnight on the dawn or dusk sides of the tail, which indeed happens later in the underlying MHD simulation.

Current diversion into both R1 and R2 type systems is found to happen inside (that is, closer to the center of the flow burst) and underneath (at lower $|z|$) the R1 and R2 type FACs, extending all the way toward the equatorial plane. This is in contrast to earlier findings (Birn & Hesse, 2005), where the diversion into R1 currents was found to occur in layers roughly parallel to the equatorial plane equatorward of the FACs but outside the equatorial plane. The apparent reason for this difference is that the earlier simulation was based on a taillike configuration, which did not include the transition toward a dipole field. In contrast to that simulation, current diversion into R1 and R2 systems takes place in dipolarized fields, which are predominantly northward. This view is supported by the fact that an additional FAC system with the signature of R0 (same sense as R2) is found in the present simulation at higher latitudes in taillike fields and that the diversion into this system takes place in layers underneath away from the equatorial plane.

A simple cartoon (Figure 1b) would suggest that the regions of current diversion (from perpendicular to field-aligned or vice versa) and generator regions, where $\mathbf{E}\cdot\mathbf{j} < 0$, are closely related. As we have shown, however, this is not necessarily so, particularly for two reasons. (1) The source region for the FACs is in the magnetotail or dipole/tail transition region, where a strong cross-tail current provides the basis from which the perturbed currents are converted to FACs. Thus, one has to consider a finite $\mathbf{j}_0$ to be superposed on the $\Delta\mathbf{j}_\perp$ vectors in Figure 1. This superposed $\mathbf{j}_0$ would be parallel to $\Delta\mathbf{j}_\perp$ on the outside of the twin vortices generated by the flow burst in the tail but antiparallel in between, that is, closer to midnight. This is, at least qualitatively, consistent with our findings of the generator regions on the outside of the R1 current system. (2) The second reason is the asymmetry of the vortical flow. The flow speed and the associated electric field are much larger inside the twin vortices (Figure 6). This leads to a net positive $\mathbf{E}\cdot\mathbf{j}$, which dominates over the negative $\mathbf{E}\cdot\mathbf{j}$ on the outside. Although the tail region covered contains the flow shear and vorticity to set up the FAC of the SCW at a magnitude commensurate with observations, it does not include the full conversion to Poynting flux that is expected prior to entry into the ionosphere. A plausible conclusion is that the conversion must continue further earthward from the region covered by the present simulation.

The present simulation did not include an ionosphere or, more precisely, a boundary condition that simulated ionospheric dissipation. That was the reason why, for the analysis of the dynamo action and energy flow and conversion, we focused on the buildup phase of the current systems, rather than a potentially

balanced generator and load circuit. We expect that this analysis would not be significantly affected if ionospheric resistance had been included, although the later evolution might be altered. An earlier study (Hesse & Birn, 1991), which included a resistive boundary condition and finite electric field at the earthward boundary, did not indicate that the dynamic evolution of the tail was significantly affected. The main effect appeared to be an earlier rise but a lower magnitude of the FACs when finite ionospheric resistance was included. But the general flow and current pattern in the tail was not significantly changed. We therefore expect that our conclusions about the current generation and diversion are not significantly altered by the absence of ionospheric dissipation.

Data Availability Statement

Simulation results are available online (via http://doi.org/10.5281/zenodo.3738460).

Acknowledgments

The simulation work was performed at Los Alamos under the auspices of the U. S. Department of Energy, supported by NASA Grants 80NSSC18K1452 and 80NSSK0834 and NSF Grant 1602655. J. E. B. was supported by NASA Heliophysics LWS TRT program via Grant NNX14AN90G and by the NSF GEM Program via Award AGS-150294. J. B. is grateful for the hospitality and support by the International Space Science Institute (ISSI), Bern, Switzerland, and the fruitful discussions with members of two ISSI working groups.

References

Amm, O., Birn, J., Bonnell, J., Borovsky, J., Carbary, J., Carlson, C., et al. (2002). Auroral plasma physics. *Space Science Reviews*, *103*, 1–475.

Birn, J. (1987). Magnetotail equilibrium theory: The general three-dimensional solution. *Journal of Geophysical Research*, *92*, 11101.

Birn, J., & Hesse, M. (1991). The substorm current wedge and field-aligned currents in MHD simulations of magnetotail reconnection. *Journal of Geophysical Research*, *96*, 1611.

Birn, J., & Hesse, M. (2005). Energy release and conversion by reconnection in the magnetotail. *Annals of Geophysics*, *23*, 3365–3373. https://doi.org/10.5194/angeo-23-3365-2005

Birn, J., & Hesse, M. (2010). Energy release and transfer in guide field reconnection. *Physics of Plasmas*, *17*, 12109.

Birn, J., & Hesse, M. (2013). The substorm current wedge in MHD simulations. *Journal of Geophysical Research: Space Physics*, *118*, 3364–3376. https://doi.org/10.1002/jgra.50187

Birn, J., & Hesse, M. (2014a). Forced reconnection in the near magnetotail: Onset and energy conversion in PIC and MHD simulations. *Journal of Geophysical Research: Space Physics*, *119*, 290–309. https://doi.org/10.1002/2013JA019354

Birn, J., & Hesse, M. (2014b). The substorm current wedge: Further insights from MHD simulations. *Journal of Geophysical Research: Space Physics*, *119*, 3503–3513. https://doi.org/10.1002/2014JA019863

Birn, J., Liu, J., Runov, A., Kepko, L., & Angelopoulos, V. (2019). On the contribution of dipolarizing flux bundles to the substorm current wedge and to flux and energy transport. *Journal of Geophysical Research: Space Physics*, *124*, 5408–5420. https://doi.org/10.1029/2019JA026658

Birn, J., Nakamura, R., Panov, E., & Hesse, M. (2011). Bursty bulk flows and dipolarization in MHD simulations of magnetotail reconnection. *Journal of Geophysical Research*, *116*, A01210. https://doi.org/10.1029/2010JA016083

Birn, J., Raeder, J., Wang, Y. L., Wolf, R. A., & Hesse, M. (2004). On the propagation of bubbles in the geomagnetic tail. *Annals of Geophysics*, *22*, 1773. https://doi.org/10.5194/angeo-22-1773-2004

Borovsky, J. E., Birn, J., Echim, M. M., Fujita, S., Lysak, R. L., Knudsen, D. J., et al. (2020). Quiescent discrete auroral arcs: A review of magnetospheric generator mechanisms. *Space Science Reviews*, *216*, 1–39. https://doi.org/10.1007/s11214-019-0619-5

Forsyth, C., Lester, M., Cowley, S. W. H., Dandouras, I., Fazakerley, A. N., Fear, R. C., & Watermann, J. (2008). Observed tail current systems associated with bursty bulk flows and auroral streamers during a period of multiple substorms. *Annals of Geophysics*, *26*(1), 167–184. https://doi.org/10.5194/angeo-26-167-2008

Fujii, R., Hoffman, R. A., Anderson, P. C., Craven, J. D., Sugiura, M., Frank, L. A., & Maynard, N. C. (1994). Electrodynamic parameters in the nighttime sector during auroral substorms. *Journal of Geophysical Research*, *99*(A4), 6093–6112. https://doi.org/10.1029/93JA02210

Gjerloev, J. W., & Hoffman, R. A. (2002). Currents in auroral substorms. *Journal of Geophysical Research*, *107*(A8), SMP 5–1-SMP 5-13. https://doi.org/10.1029/2001JA000194

Hamrin, M., Marghitu, O., Rönnmark, K., Klecker, B., André, M., Buchert, S., & Vaivads, A. (2006). Observations of concentrated generator regions in the nightside magnetosphere by Cluster/FAST conjunctions. *Annals of Geophysics*, *24*(2), 637–649. https://doi.org/10.5194/angeo-24-637-2006

Henderson, M. G., Murphree, J. S., & Reeves, G. D. (1998). Are north-south aligned auroral structures the ionospheric manifestations of bursty bulk flows? *Geophysical Research Letters*, *25*, 3737.

Hesse, M., & Birn, J. (1991). Magnetosphere-ionosphere coupling during plasmoid evolution: First results. *Journal of Geophysical Research*, *96*(A7), 11,513–11,522. https://doi.org/10.1029/91JA00440

Hesse, M., & Birn, J. (1993). Three-dimensional magnetotail equilibria by numerical relaxation techniques. *Journal of Geophysical Research*, *98*, 3973.

Iijima, T., & Potemra, T. A. (1976). The amplitude distribution of field-aligned currents at northern high latitudes observed by Triad. *Journal of Geophysical Research*, *81*, 2165.

Keiling, A., Angelopoulos, V., Runov, A., Weygand, J., Apatenkov, S. V., Mende, S., & Auster, H. U. (2009). Substorm current wedge driven by plasma flow vortices: THEMIS observations. *Journal of Geophysical Research*, *114*, A00C22. https://doi.org/10.1029/2009JA014114

Kepko, L., McPherron, R. L., Amm, O., Apatenko, S., Baumjohann, W., Birn, J., & Sergeev, V. (2015). Substorm current wedge revisited. *Space Science Reviews*, *190*, 1–46. https://doi.org/10.1007/s11214-014-0124-9

Liu, J., Angelopoulos, V., Runov, A., & Zhou, X. Z. (2013). On the current sheets surrounding dipolarizing flux bundles in the magnetotail: The case for wedgelets. *Journal of Geophysical Research: Space Physics*, *118*, 2000–2020. https://doi.org/10.1002/jgra.50092

Liu, Y. H., Birn, J., Daughton, W., Hesse, M., & Schindler, K. (2014). Onset of reconnection in the near magnetotail: PIC simulations. *Journal of Geophysical Research: Space Physics*, *119*, 9773–9789. https://doi.org/10.1002/2014JA020492,_2014

Lyons, L. R., Nagai, T., Blanchard, G. T., Samson, J., Yamamoto, T., Mukai, T., & Kokubun, S. (1999). Association between Geotail plasma flows and auroral poleward boundary intensifications observed by CANOPUS photometers. *Journal of Geophysical Research*, *104*, 4485.

Marghitu, O., Hamrin, M., Klecker, B., Vaivads, A., McFadden, J., Buchert, S., & Rème, H. (2006). Experimental investigation of auroral generator regions with conjugate Cluster and FAST data. *Annals of Geophysics*, *24*(2), 619–635. https://doi.org/10.5194/angeo-24-619-2006

McPherron, R. L., Russell, C. T., & Aubry, M. A. (1973). Satellite studies of magnetospheric substorms on August 15, 1968, 9, Phenomenological model for substorms. *Journal of Geophysical Research*, *78*, 3131.

Merkin, V. G., Panov, E. V., Sorathia, K. A., & Ukhorskiy, A. Y. (2019). Contribution of bursty bulk flows to the global dipolarization of the magnetotail during an isolated substorm. *Journal of Geophysical Research: Space Physics*, *124*, 8647–8668. https://doi.org/10.1029/2019JA026872

Nakamura, R., Baumjohann, W., Brittnacher, M., Sergeev, V. A., Kubyshkina, M., Mukai, T., & Liou, K. (2001). Flow bursts and auroral activations: Onset timing and foot point location. *Journal of Geophysical Research*, *106*, 10,777–10,789.

Nakamura, R., Baumjohann, W., Schödel, R., Brittnacher, M., Sergeev, V. A., Kubyshkina, M., & Liou, K. (2001). Earthward flow bursts, auroral streamers, and small expansions. *Journal of Geophysical Research*, *106*, 10,791–10,802.

Nakamura, R., Nagai, T., Birn, J., Sergeev, V. A., Contel, O. L., Varsani, A., et al. (2017). Near-Earth plasma sheet boundary dynamics during substorm dipolarization. *Earth Planets Space*, *69*(129), 1–14. https://doi.org/10.1002/2017JA024686

Nakamura, R., Varsani, A., Genestreti, K. J., Le Contel, O., Nakamura, T., Baumjohann, W., & Turner, D. L. (2018). Multiscale currents observed by MMS in the flow braking region. *Journal of Geophysical Research: Space Physics*, *123*, 1260–1278. https://doi.org/10.1002/2017JA024686

Scholer, M., & Otto, A. (1991). Magnetotail reconnection: Current diversion and field-aligned currents. *Geophysical Research Letters*, *18*, 7331.

Sergeev, V. A., Liou, K., Meng, C. I., Newell, P. T., Brittnacher, M., Parks, G., & Reeves, G. D. (1999). Development of auroral streamers in association with localized impulsive injections to the inner magnetotail. *Geophysical Research Letters*, *26*, 417.

Sergeev, V., Liou, K., Newell, P. T., Ohtani, S. I., Hairston, M. R., & Rich, F. (2004). Auroral streamers: Characteristics of associated precipitation, convection and field-aligned currents. *Annales Geophysicae*, *22*, 537.

Sitnov, M. I., Swisdak, M., & Divin, A. V. (2009). Dipolarization fronts as a signature of transient reconnection in the magnetotail. *Journal of Geophysical Research*, *114*, A04202. https://doi.org/10.1029/2008JA013980

Wiltberger, M., Merkin, V., Lyon, J. G., & Ohtani, S. (2015). High-resolution global magnetohydrodynamic simulation of bursty bulk flows. *Journal of Geophysical Research: Space Physics*, *120*, 4555–4566. https://doi.org/10.1002/2015JA021080